A fluorescence-electrochemical study of carbon nanodots (CNDs) in bio- and photoelectronic applications and energy gap investigation

By: Zheng Zeng, Wendi Zhang, Durga M. Arvapalli, Brian Bloom, Alex Sheardy, Taylor Mabe, Yiyang Liu, Zuowei Ji, Harish Chevva, David H. Waldeck, and Jianjun Wei

Z. Zeng, W. Zhang, D. Arvapalli, B. Bloom, A. Sheardy, T. Mabe, Y. Liu, Z. Ji, H. Chevva, D. Waldeck, J. Wei, A Fluorescence-Electrochemical Study of Carbon Nanodots (CNDs) for Bio- and Photoelectronic Application and Energy Gap Investigation, *Physical Chemistry Chemical Physics (PCCP)*, **2017**, 19, 20101-20109. http://www.doi.org/10.1039/C7CP02875J

Abstract:

Carbon nanodots (CNDs) have attracted great attention due to their superior solubility, biocompatibility, tunable photoluminescence, and opto-electronic properties. This work describes a new fluorescence-based spectroelectrochemistry approach to simultaneously study the photoluminescence and wavelength dependent photocurrent of microwave synthesized CNDs. The fluorescence of CNDs shows selective quenching upon a reversible redox couple, ferricyanide/ferrocyanide, reaction during cyclic voltammetry. The CND modified gold slide electrode demonstrates wavelength dependent photocurrent generation during the fluorescence-electrochemical study, suggesting the potential application of CNDs in photoelectronics. UV-Vis absorption and electrochemistry are used to quantify the energy gap of the CNDs, and then to calibrate a Hückel model for CNDs' electronic energy levels. The Hückel (or tight binding) model treatment of an individual CND as a molecule combines the conjugated π states (C=C) with the functional groups (C=O, C–O, and COOH) associated with the surface electronic states. This experimental and theoretical investigation of CNDs provides a new perspective on the optoelectronic properties of CNDs and should aid in their development for practical use in biomedicine, chemical sensing, and photoelectric devices.

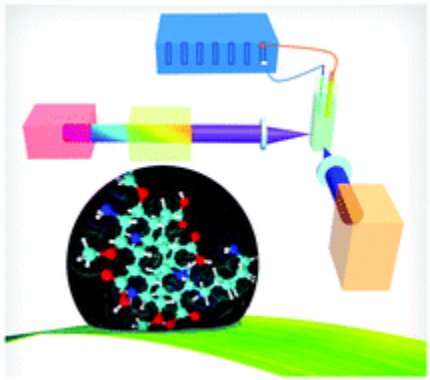

Keywords: Carbon nanodots (CNDs) | fluorescence spectroelectrochemistry |

Article:

Introduction

Carbon-based nanodots (CNDs) are reported to be composed of polyatomic carbon domains surrounded by amorphous carbon frames and have been synthesized by chemical ablation, electrochemical carbonization, laser ablation, hydrothermal/solvothermal treatment, and microwave irradiation techniques.[1,2] There is continued interest in CNDs because of their physicochemical properties of good solubility, low toxicity, and biocompatibility, along with their favorable optoelectronic properties of strong fluorescence, phosphorescence, chemiluminescence, and photoinduced electron transfer.[2–6] As such, CNDs have been found to have potential applications in biomedicine (bioimaging, biosensor, and biomedicine delivery system), chemical sensing, and photoelectric devices (solar cells, supercapacitors, photocatalysis and light-emitting devices).[2–4] To explain the mechanism of light emission in CNDs,[7,8] some workers have proposed that the bandgap transitions responsible for fluorescence arise from conjugated π-domains consisting of sp^2 hybridized islands rich in π-electrons, bond disorder induced energy gaps,[9,10] or giant red-edge effects that give rise to strong excitation wavelength dependent fluorescence.[11,12] These mechanisms are similar to those used to understand the emissive properties of single-layer graphene and graphene oxides.[13,14] Other workers ascribe the light emission characteristics to quantum confinement effects,[15] size-dependent optical properties,[16] surface-related defect sites,[17] and radiative recombination of excited surface states.[18] The lack of consensus on the relevant photophysical properties of CNDs is likely caused by variations in CND size and surface state properties, resulting from the many different synthetic routes used in their preparation. A poor understanding of the structure of CNDs in terms of their functional groups, defects, adsorbates, and electronic structure continues to impede the development of an agreed upon mechanism.

This work uses a new combined fluorescence-electrochemical approach to investigate the optoelectronic properties of CNDs. Although numerous spectroelectrochemical techniques have been developed, such as electrochemical fluorescence spectroscopy,[19,20] electrochemical surface/tip-enhanced Raman spectroscopy,[21,22] and ultraviolet-visible (UV-Vis) absorption spectroelectrochemistry,[23,24] the simultaneous study of fluorescence and electrochemical measurements which focus on the effect of chemically reversible reactions on CNDs is rare. Here, water-soluble luminescent CNDs were synthesized by a simple one-step microwave route and were characterized by transmission electron microscopy (TEM), atomic force microscopy (AFM), X-ray photoelectron spectroscopy (XPS), Fourier transform infrared spectroscopy (FTIR), Raman spectroscopy, X-ray powder diffraction (XRD), UV-Vis spectroscopy, fluorescence spectroscopy, pH dependent zeta potential measurements, and quantum yield measurements. Their potential application in bioimaging was assessed from their excitation-dependent fluorescence, and their potential use as chemiluminescent sensors was evaluated by examining the effect of the ferricyanide/ferrocyanide redox couple on their fluorescence spectrum. We also examined the excitation wavelength dependence of the photocurrent (action spectrum) generated by CNDs that were immobilized on gold slide electrodes to assess their potential application in photoelectric devices. Optical and electrochemical measurements were used to measure the energy gap of the CNDs, and Hückel level calculations of the HOMO

(highest occupied molecular orbital) and LUMO (lowest unoccupied molecular orbital) were fitted to the energy gap measurements by treating a CND as a molecule.

Materials and methods

Synthesis of CNDs

A microwave assisted synthesis of CNDs was performed using citric acid and urea as precursors.[25] Briefly, 1.0 g of urea (Aldrich) and 1.0 g of citric acid (ACROS Organics) were simultaneously added to 1.0 mL of deionized water to form a homogeneous solution and then heated in a microwave synthesizer (CEM Corp 908005 Microwave Reactor Discovery System) at a power of 150 W for 12 minutes. After cooling, the aqueous reaction mixture was purified using a centrifuge (Solvall Legend XFR Floor Model Centrifuge) at 3500 rpm for 20 minutes to remove large and aggregated particles. The dark-brown solution was further purified using a dialysis membrane (Fisher Scientific) with a molecular weight cut off of 1000 Da for 24 hours. To obtain the solid sample, the resulting solution was finally dried using a freeze dryer (Labconco Free Zone 6 Freeze Dryer) for 24 hours.

Characterization of CNDs

Atomic force microscopy (AFM, Agilent Technologies 5600 LS Series) and transmission electron microscopy (TEM, Carl Zeiss Libra 120 Plus) were used to study the size of the CNDs. Fourier transform infrared spectroscopy (FTIR, Varian 670), Raman spectroscopy (Horiba XploRA One Raman Confocal Microscope System), X-ray photoelectron spectroscopy (XPS, Thermo Fisher ESCALAB 250 Xi), and X-ray powder diffraction (XRD, Agilent Technologies Oxford Gemini) were used to determine the elemental composition and chemical structure of the CNDs. A Zetasizer nano-ZX (Malvern Instruments ZEN3600) was used to study the stability of the CNDs as a function of pH (Fisher Scientific pH 2100). Ultraviolet-visible spectroscopy (UV-Vis spectroscopy, Varian Cary 6000i) and fluorescence spectroscopy (Varian Cary Eclipse) were used to investigate the absorbance and fluorescence properties of the CNDs, respectively.

Cell culture and bioimaging

HepG2 cells were obtained from American Type Culture Collection (ATCC) and cultured in Eagle's minimum essential medium [2 mM l-glutamine, 1 mM sodium pyruvate, and 1500 mg L^{-1} sodium bicarbonate] (ATCC) containing 10% fetal bovine serum (Fisher Scientific, USA), 1% antibiotic with 100 UI mL^{-1} penicillin and 100 μg mL^{-1} streptomycin (Fisher Scientific, USA). The cells were incubated in a humidified incubator with 5% CO_2 at 37 °C. Trypsin/EDTA (Fisher Scientific, USA) was used to passage the cells serially. The cells were seeded (150 000 cells per dish) in petri dishes containing cover slips. After culturing for 24 hours, the cells were treated with CNDs at a concentration of 0.3 mg mL^{-1}. Untreated cells without CNDs were used as control. The cells were imaged using a confocal microscope (Carl Zeiss Libra 120 Plus Z1) by mounting the cover slips onto glass slides. All the images were taken at 10× magnification and at a scale bar of 20 μm.

Fluorescence spectroelectrochemistry

The electrochemical-fluorescence technique comprises a Bio-logic VMP3 electrochemical workstation with a two-electrode testing system where a platinum wire was used as the counter electrode and a gold electrode (Fisher Scientific) for the fluorescence spectroelectrochemistry experiment as the working electrode (replaced by a CND immobilized gold slide electrode for the photocurrent generation experiment) and a fluorescence spectrophotometer whose excitation wavelength could be varied from 200 to 700 nm by using a 450 W xenon lamp with an excitation monochromator (the area of illumination is about 5 mm in diameter) and emission could be collected from 300 to 1000 nm by using an emission monochromator (Agilent).

Preparation of immobilized CNDs at gold slide electrode surfaces

The gold coated slides (20 nm Au deposited on 8 mm × 8 mm glass slides by physical vapor deposition (Kurt Lesker PVD75 E-Beam Evaporator System)) were first cleaned with O_2 plasma (South Bay Technologies PC2000 Plasma Cleaner) for 15 minutes. The slides were then incubated in a mixture of 1 mM 11-mercaptodecanoic acid (HSC10COOH, Aldrich) and 8-mercapto-octanol (HSC8OH, Aldrich) in absolute ethanol solution (ACROS Organics) with a 1 : 5 mole ratio overnight to form a self-assembled monolayer (SAM) by alkyl thiols. After SAM formation, the gold slides were incubated in 0.5 mM 1-(3-dimethylaminopropyl)-3-ethylcarbodiimide hydrochloride (EDC, TCI)/*N*-hydroxysuccinimide (NHS, Aldrich) for 2 hours to activate the carboxylic acid groups.[26,27] Next, the gold slides were rinsed with deionized water and immediately moved to a freshly prepared 3 mL solution containing 0.3 mg mL^{-1} of CNDs for 2 hours. The gold slides were rinsed with deionized water and dried before experiments.

Energy gap and molecular orbital energy level calculation

The optical band gap was determined using an indirect band gap calculation.[28] The UV-Vis absorption spectrum calculation was performed by plotting $\sqrt{Ahv}$ *versus* hv, where A is the measured absorbance, h is the Planck constant, v is the frequency, and hv is equal to 1240/wavelength in units of eV. $\sqrt{Ahv}$ has a linear relationship with hv with a slope of D and the optical band gap is the x-intercept. Cyclic voltammetry (CV) was used to obtain the HOMO and LUMO energy levels of the CNDs.[29] The electrochemical measurement was performed using a three-electrode electrochemical cell with a gold working electrode, a Ag/AgCl reference electrode, and a platinum counter electrode (Fisher Scientific) in a 4.0 mL acetonitrile (Fisher Scientific) solution containing 0.1 M tetrabutylammonium hexafluorophosphate (Fisher Scientific) as the supporting electrolyte and 1 mL of deionized water containing 0.3 mg of CNDs. Cyclic voltammetry of the sample was run at a scan rate of 100 mV s^{-1} under room temperature. The electrochemical data were used to determine the HOMO and LUMO energy levels; namely, $E_{HOMO} = -(E_{onset,ox} + 4.66)$ eV, and $E_{LUMO} = -(E_{onset,red} + 4.66)$ eV, where $E_{onset,ox}$ and $E_{onset,red}$ are the onset of the oxidation and reduction potentials,[29] respectively (note that the formal potential of the Fc^+/Fc redox couple was estimated as −5.06 eV in the Fermi scale when the formal potential of the Fc^+/Fc redox is 0.40 V *versus* Ag/AgCl. See details in ESI†). The Hückel method was used to reproduce the energy gap by assuming a molecular structure of CNDs and adjusting the coulomb and resonance integral values to obtain a HOMO–LUMO gap that is consistent with the energy gap values obtained from the spectral and electrochemical

measurements.[30] These parameters were used to calculate the different molecular orbital energy levels (see details in ESI†).

Results and discussion

CND synthesis and characterization

A one-step microwave route was used to synthesize CNDs from citric acid and urea.[25] Transmission electron microscopy (Fig. 1A) and atomic force microscopy (Fig. 1B), with associated height profile analyses (Fig. S1, ESI†), indicate that the CNDs are spherical and well dispersed, and have an average size of about 3 nm. FTIR spectra of the CNDs (Fig. 1C) display broad bands at 3100–3400 cm^{-1} which are assigned to ν(O–H) and ν(N–H) functionalities that help explain the hydrophilicity and stability of the CNDs in aqueous media. The IR transitions at 768, 1184, 1402 and 1566 cm^{-1} are assigned to ν(C–C), ν(C–O), ν(C=C) and ν(C=O), respectively.[31] The presence of these functionalities at the surfaces is corroborated by XPS data (Fig. 1D) of the CNDs, which could be fitted by four components: C=C and C–C (49.8%, 284.8 eV), C=O (36.6%, 287.8 eV), C–O (7.3%, 286.5 eV), and COOH (6.3%, 289.0 eV). Associated with the high-resolution O (Fig. S2 and Table S1, ESI†) and N (Fig. S3 and Table S2, ESI†) XPS spectra and their simulated peak fits, the survey XPS spectrum analysis shows the atomic ratio of C : O : N to be 54 : 27 : 17 (Table S3, ESI†). Raman spectra of the CNDs (Fig. 1E) show both D bands at 1341 cm^{-1} (sp^3-hybridized) and G bands at 1564 cm^{-1} (sp^2-hybridized) with an intensity ratio I_D/I_G of about 1.06, suggesting the presence of a disordered graphite structure.[32,33] The main diffraction peak in the XRD spectrum (Fig. 1F) appears at 25.2° with a full width at half maximum (FWHM) of about 3.2°, which corresponds to an interlayer distance of 0.35 nm between the planar carbon based sheets for the graphite structure region.[34] The zeta potential of the CNDs was −22.3 mV at a pH of 5.86 (Table S4, ESI†), owing to the presence of carboxylate groups on the surface, further corroborating that the CNDs are highly dispersed and stable in the aqueous system.[35,36] In summation, the structure of the CNDs in this study is spheroidal with an average size of 3 nm and consists of a disordered graphite structure with surrounding amorphous carbon frames and functional groups on the surfaces.

Fig. 1G shows the absorption spectrum of the CNDs over the spectral range of 200 to 600 nm. There is no obvious absorption feature found above 600 nm. A shoulder/peak in the spectrum at about 236 nm is consistent with π–π* transitions of C–C and C=C bonds in sp^2 hybrid regions and the main peak at 331 nm is consistent with n–π* transitions of the C=O moieties.[37,38] The emission of the CNDs occurs over a spectral region from 400 nm to wavelengths longer than 600 nm (see Fig. 2A). Relative quantum yield measurements, using quinine sulfate as the reference, give a quantum yield of 8.5% (Table S5, ESI†) for the as-prepared CNDs.[39] Other than the lack of a well-defined vibronic structure, these spectra are consistent with that expected for large π-conjugated catacondensed hydrocarbons.

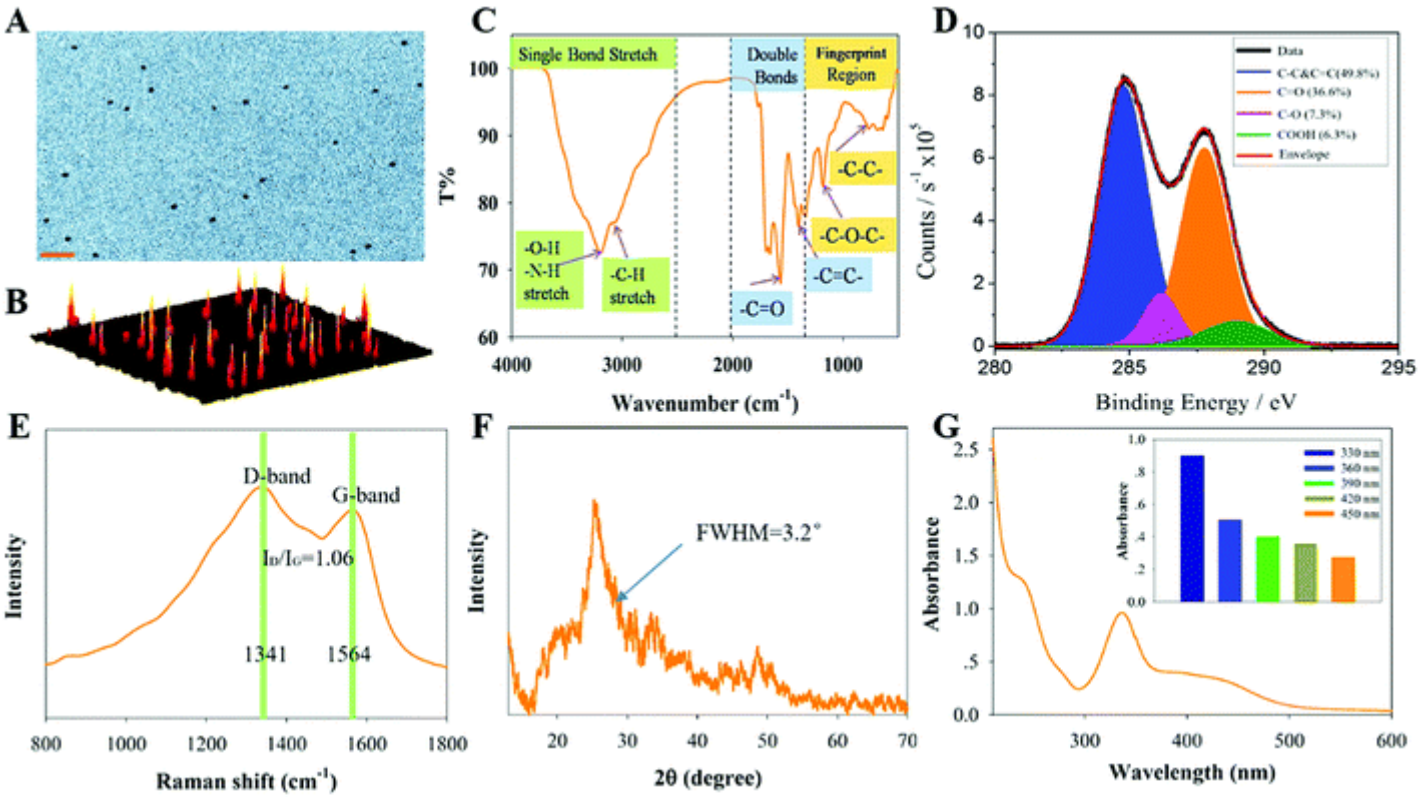

Fig. 1 The CNDs are characterized using different techniques: (A) transmission electron micrograph (scale bar is 20 nm), (B) atomic force microscopy profile of CNDs distributed on a mica surface, (C) Fourier transform infrared spectrum, (D) X-ray photoelectron spectrum (C signal), (E) Raman spectrum, (F) X-ray diffraction data, and (G) UV-Vis absorption spectrum of CNDs.

CND fluorescence and cell imaging

CNDs can act as blue/green fluorophores in imaging applications.[40] Fig. 2A shows the fluorescence emission spectra of the synthesized CNDs in deionized water at five different excitation wavelengths (λ_{ex} = 330, 360, 390, 420, and 450 nm). The maximum emission intensity occurs with 360 nm excitation and has a peak emission at 454 nm. The apparent red-shift in the photoluminescence spectra with the change in excitation wavelength is in agreement with other reports.[41,42] The potential application of CNDs as a bioimaging agent is confirmed by the uptake of fluorescent CNDs by HepG2 cells.[43] Spinning disk confocal microscopy was used to monitor the cellular uptake phenomenon by HepG2 cells after treatment with CNDs for 24 hours (Fig. 2). The strong blue and green fluorescence indicates that the CNDs are internalized by the HepG2 cells (for more details, see Fig. S4, ESI†). Furthermore, the cells were grown in the presence of CNDs (0.3 mg mL^{-1}) for 72 hours without any significant cytotoxicity (Fig. S4, ESI†). The strong blue and green fluorescence was consistent with the calculation of chromaticity coordinates (CIE Chromaticity Diagram) that was performed after inputting the emission data obtained from excitation at 330 nm and 450 nm. These results suggest that the as-prepared CNDs are good candidates for use as cell imaging agents.

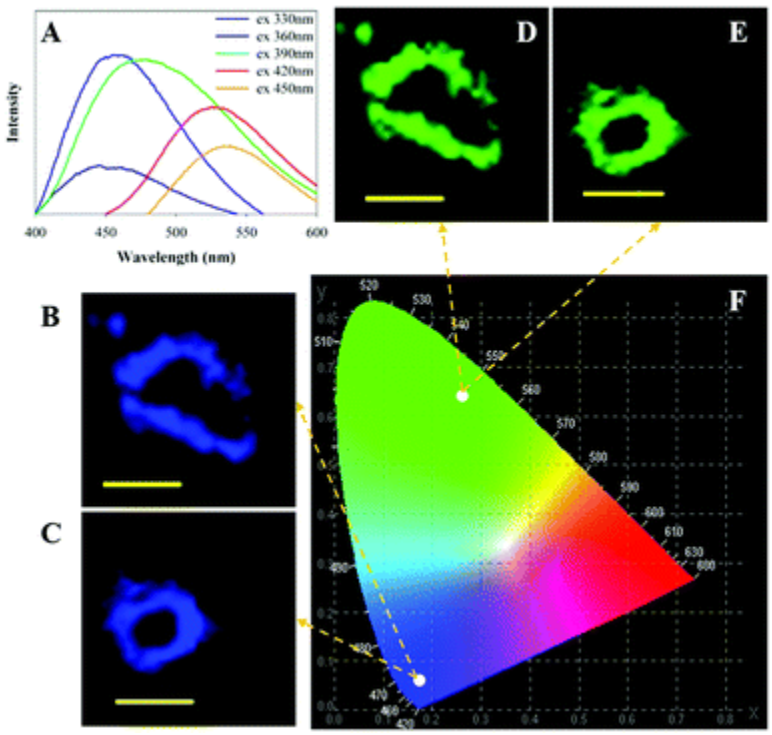

Fig. 2 (A) Fluorescence emission spectra of CNDs in deionized water. (B and C) Confocal images of HepG2 cells that are cultured with CNDs (0.3 mg mL^{-1}) for 24 hours, taken at 330 nm excitation. All of the images have a scale bar of 20 μm. (D and E) Confocal images as in panels B and C, but with 450 nm excitation. (F) Calculation of chromaticity coordinates with the emission results under excitation wavelengths of 330 and 450 nm.

Fluorescence spectroelectrochemistry

A ferricyanide/ferrocyanide redox couple was chosen as the redox probe for spectroelectrochemical measurements because it is a reversible system with spectroscopically distinguishable redox forms.[44,45] Fig. 3A shows cyclic voltammograms (CV) of a ferri-/ferrocyanide solution at scan rates of 10, 20, 50, and 100 mV s^{-1}. Fig. 3B shows the fluorescence intensity of the CND solution (using 360 nm excitation) with increasing potassium ferricyanide ($K_3Fe(CN)_6$) concentration. At low concentrations (<33 μM) of $K_3Fe(CN)_6$ the fluorescence of the CNDs is not affected strongly; however, from 33 μM to 333 μM of $K_3Fe(CN)_6$, the fluorescence intensity of the CNDs decreases and the emission peak red-shifts. This fluorescence quenching can arise from two phenomena. The main contributing factor is the reaction of CNDs with $Fe(CN)_6^{3-}$ (CNDs + $Fe(CN)_6^{3-}$ → CNDs* + $Fe(CN)_6^{4-}$) which may influence the surface electronic state transitions caused by incomplete passivation. Since the energy gap of surface states is larger than that of the core states (details are shown in the energy gap calculation part) and smaller energy gap induces larger emission wavelength, the red-shift of the fluorescence peaks occurs with increasing concentrations of $K_3Fe(CN)_6$.[46,47] The other factor is probably an optical filtering effect caused by ferricyanide that absorbs light at a peak wavelength of 420 nm, while ferrocyanide does not (Fig. S5, ESI†). Note that the fluorescence spectrum of CNDs before and after the addition of various concentrations of ferrocyanide does not change (Fig. S6, ESI†), suggesting that the redox process between $K_4Fe(CN)_6$ and

$K_3Fe(CN)_6$ (the oxidation of ferrocyanide to ferricyanide and the reduction of ferricyanide to ferrocyanide) is responsible for the change in the fluorescence intensity of the CNDs.

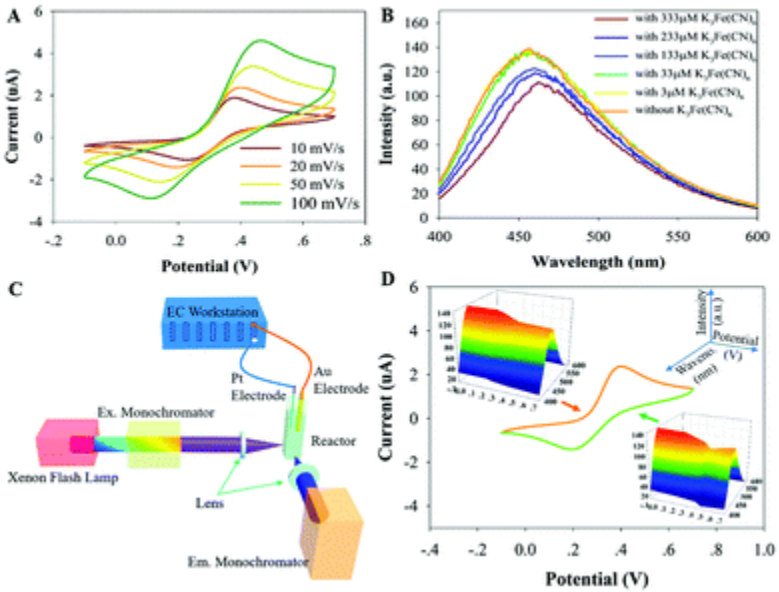

Fig. 3 (A) Cyclic voltammogram (CV) of a mixture of 333 μM $K_4Fe(CN)_6$ and 0.1 M KCl solution between −0.1 V and 0.7 V at 10, 20, 50 and 100 mV s^{-1} scan rates. (B) Fluorescence spectrum of the solution including 50 μg mL^{-1} CNDs and 0.1 M KCl after the addition of $K_3Fe(CN)_6$ with different concentrations (3, 33, 133, 233, and 333 μM). (C) Schematic view of the setup used for coupling electrochemistry with fluorescence spectroscopy. (D) CV of 333 μM $K_4Fe(CN)_6$ in 0.1 M KCl between −0.1 V and 0.7 V at a scan rate of 20 mV s^{-1} with the inserted three-dimensional spectra of the fluorescence signal of CNDs during the CV experiment (the solution includes 50 μg mL^{-1} CNDs, 333 μM $K_4Fe(CN)_6$, and 0.1 M KCl).

To record voltammograms for $K_4Fe(CN)_6$ and the concurrent, real-time influence of $K_3Fe(CN)_6$ on the fluorescence properties, a scan rate of 20 mV s^{-1} and 333 μM $K_4Fe(CN)_6$ were selected for the fluoro-electrochemical studies (see Fig. 3C and D). Fig. 3D shows the fluoroelectrochemical data for the redox cycling of ferrocyanide and ferricyanide. As ferrocyanide is oxidized to ferricyanide near 0.45 V (*vs.* Ag/AgCl), the fluorescence peaks of the CNDs decrease (Fig. 3D). In addition, the fluorescence peaks of the CNDs increase in the potential range from 0.45 to 0.2 V (*vs.* Ag/AgCl) on the reverse scan, suggesting the consumption of the electrogenerated ferricyanide. Note that, from 0.2 V of the reverse scan up to 0.24 V of the forward scan, the fluorescence peaks of CNDs are about 98.5% of that shown in Fig. S6 (ESI†). In summary, these results demonstrate that the CNDs can be used as a chemiluminescence sensor for obtaining electrochemical properties using fluorescence spectrometry.

Photocurrent generation from a CND immobilized gold slide

The immobilization of CNDs on the gold slide surface was verified by AFM (Fig. S1, ESI†). The CNDs are clearly visualized as white spots in the AFM image. Following a similar analysis to the one for analysing immobilized proteins on an alkyl thiol SAM,[48] a detailed analysis of the

spots of the AFM image indicates that CNDs are uniformly distributed on the slide surface with a surface coverage of about 26.3 ± 0.6% of the slide surface area. By subtracting the average height of the white spots (~6 nm) from the thickness of -SC10CO-SAM (1–1.1 nm) and roughness of the gold slide (1–2 nm), the thickness of CNDs is estimated to be about 3 nm (Fig. S1, ESI†), which is consistent with the results obtained by TEM and AFM images of CNDs on mica surface (Fig. 1), suggesting a monolayer of CNDs has been immobilized on the gold surface covalently linked to the -SC10CO-SAM.

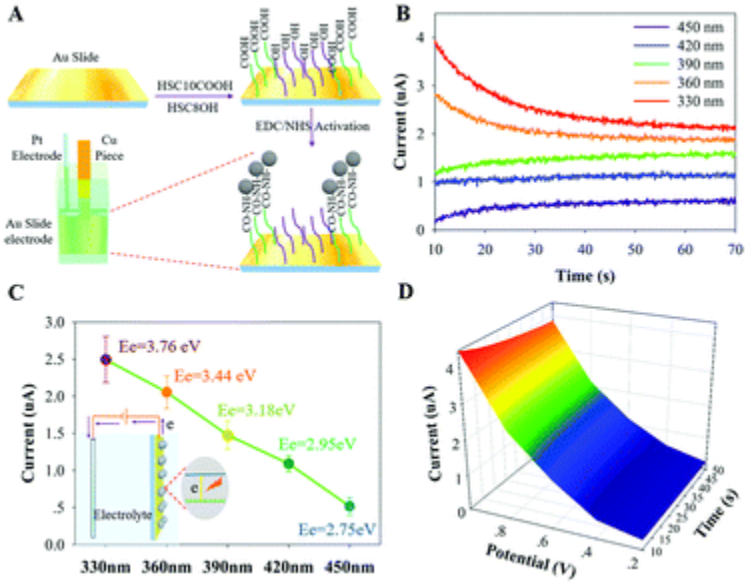

Fig. 4 (A) Illustration of the protocol for self-assembled monolayer (SAM) formation and CND immobilization on the gold slide electrode. Note that the fluoro-electrochemical setup is the same as that in Fig. 3C except that the gold electrode was changed to the CND immobilized gold slide electrode which is electrically connected through a piece of copper tape. (B) Chronoamperometry (CA) photocurrent measurements of CNDs immobilized on the electrode at an applied voltage of 0.8 V. The different irradiation wavelengths are shown in the legend, ranging from 330 to 450 nm. (C) The long time photocurrent of the CND films is plotted for the different incident wavelengths, with photon energy, $E_e = hc/\lambda$, indicated. The inset shows a schematic view of photocurrent generation of CNDs upon excitation. (D) The chronoamperometry measurement with different applied bias potentials of the gold slide electrode with CND immobilization under an incident wavelength of 330 nm.

The action spectrum of the CNDs immobilized on a gold slide electrode (Fig. 4A) was obtained by measuring the photocurrent in 3 mL of 0.1 M Na_2SO_4 electrolyte solution under monochromatic light irradiation. The Na_2SO_4 based electrolyte solution was N_2-degassed before the photocurrent experiment. Fig. 4B shows the photocurrent measurements (at an applied voltage of 0.8 V) of the CND treated electrodes at five different irradiation wavelengths (Fig. S7 and S8 (ESI†) show the chronoamperometry (CA) measurement and a control experiment for the untreated gold slide electrode). Note that the resulting current from the photo-excitation processes occurring at the electrode was monitored as a function of time by the CA measurement in which the potential of the working electrode from chronoamperometry is stepped, and after 50 seconds of decay time from the initial to the steady-state current, we calculated the net photocurrent attributed by CNDs (as shown in Fig. 4D) by subtracting CA measurements with an

applied voltage of 0.8 V of the gold slide electrode without CND immobilization (Fig. S8, ESI†) from CA measurements of the gold slide electrode with CND immobilization (Fig. S7, ESI†) before and after light irradiation with different incident wavelengths (330–450 nm). The highest photocurrent (~2.5 μA) was obtained for an incident wavelength of 330 nm (corresponding to photon energy, E_e = 3.76 eV) while the lowest photocurrent (~0.5 μA) was obtained for an incident wavelength of 450 nm (E_e = 2.75 eV) (Fig. 4C). Since no photocurrent was observed from the bare gold electrode under the photo-excitation process, the photocurrent action spectrum demonstrates that the CNDs are the photoactive species responsible for photocurrent generation. Since the intensity of incident light is independent of its wavelength, the incident wavelength dependent photocurrent generation by CNDs may be arising from two likely factors. The first is an increase in the incident photon to charge carrier efficiency that arises from higher light absorbance of CNDs at shorter wavelengths, as concluded from their absorption spectrum (Fig. 1G inset),[49] and the second is the somewhat higher energy of the photoinjected electrons at shorter wavelengths.

In analogy to a semiconductor–electrolyte interface, CNDs generate electron–hole pairs (e^-–h^+) that can then follow various relaxation pathways, including electron–hole pair radiative recombination, charge transfer to the substrate, and charge transfer to an acceptor in the electrolyte.[50–52] The photocurrent measured in this system, without a redox couple in solution, corresponds to a net electron transfer from the CNDs to the gold slide electrode; thus the photocurrent is anodic. Fig. 4D and Fig. S9 (ESI†) show that the voltage dependence of the photocurrent generated by the CNDs under excitation at 330 nm increases monotonically with increasing positive bias.

It was observed that the photocurrent decays with time especially under high energy incident light (330 nm) at high bias voltage (0.8 V). To examine if there was degradation of the CND layer at the gold slide electrode, multiple photocurrent measurements were carried out at different times using the same electrode; no significant changes in the magnitude of the photocurrents were observed, suggesting the stability of the CND layer at the gold slide electrode. The decay of photocurrent with time (~50 s to become stable) may be attributed to the need for establishing an equilibrium status of the semiconductor–electrolyte interface. Under the light excitation with higher energy, the more electron–hole pair (e^-–h^+) separation at the interface (coupling with a double layer capacitance behavior with an external electrical field) would take longer time (see Fig. S7, ESI†) to reach the equilibrium status for stable photocurrent generation. More insightful understanding (*e.g.* electron–hole pair generation and recombination, charge transfer, and analysis of mobility in CNDs) of the photocurrent decay would be of great interest for a real photovoltaic device development, which, however, is beyond the scope of this study.

The increase in photocurrent at higher bias potentials can be explained using a Fowler–Nordheim model[53] for the photocurrent. In this model, the photocurrent is proportional to the following dimensionless tunnelling probability:[53]

$$I_p \propto \exp\left[-\frac{4}{3}\frac{\sqrt{2m^*}}{qh}\frac{\Phi_B^{3/2}L}{V_0 + \propto V_a}\right] \quad (1)$$

where I_p is the photocurrent, q is the electron charge, h is Planck's constant, m^* is the effective mass, Φ_B is the tunnelling barrier height, V_0 is the open circuit voltage, αV_a is the fraction of the applied voltage across the barrier (thus affecting the electric field), and L is the length over which the electric field applies. Hence, higher applied bias voltages result in a higher photocurrent from the CNDs. The photoinduced excitation and subsequent charge transport to the gold slide electrode demonstrate the potential of CNDs in photovoltaic and other optoelectronic device applications.

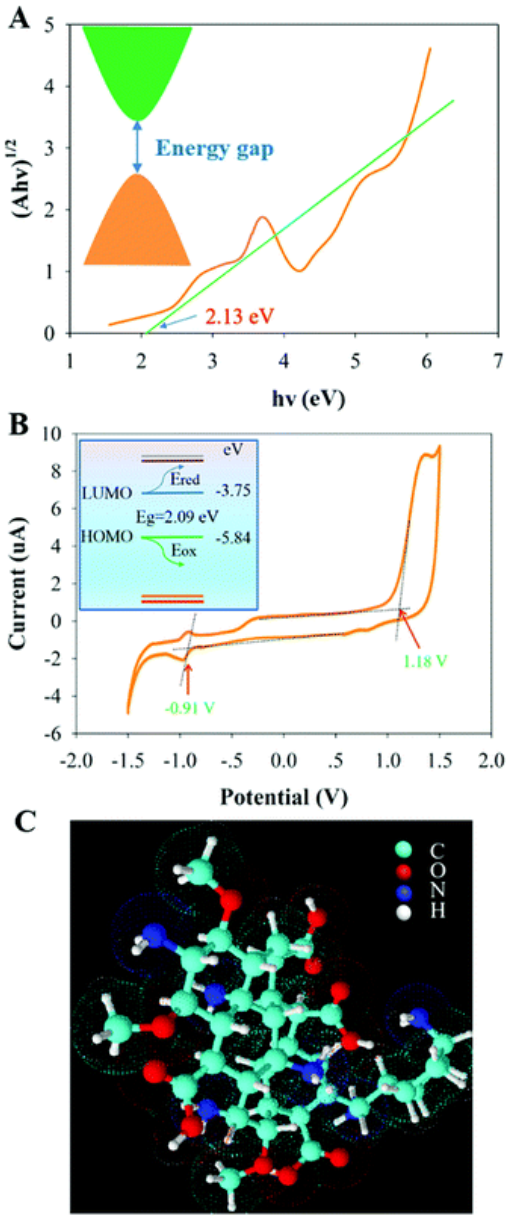

Fig. 5 (A) UV-Vis absorption spectrum of the CNDs used to estimate the optical band gap (E_0). (B) A cyclic voltammogram of the CNDs is shown, and the inset illustrates its relation to the energy levels. (C) A proposed molecule-like structure (with the formula $C_{36}H_{58}N_6O_{11}$) of individual CNDs based on the characterization results.

Energy gap investigation and analysis

The electronic energy levels of the carbon atoms combine to form delocalized bands of energy states,[54] including a valence band maximum (in analogy to HOMO) and a conduction band minimum (in analogy to LUMO). From the UV-Vis absorption spectrum (Fig. 1G), the optical band gap E_0 of the CNDs is estimated to be 2.13 ± 0.06 eV (Fig. 5A).[28] After adjusting for the exciton binding energy E_b (about 6.1–13.6 meV),[55,56] the energy gap from the optical measurement is estimated to be about 2.12 ± 0.06 eV. In addition, electrochemical measurements can be used to determine the HOMO and LUMO positions by treating an individual CND as a molecule. The onsets of the reduction (E_{red}) and oxidation (E_{ox}) potentials for the CNDs give energies of −3.75 ± 0.04 eV of the LUMO energy level and −5.84 ± 0.04 eV of the HOMO energy level, respectively (Fig. 5B and Fig S10, ESI†). These values give an HOMO–LUMO energy gap for the CNDs of 2.09 ± 0.08 eV,[29,57] which is close to the energy gap value obtained from the spectral measurements.

The Hückel method[30] was used to calculate the molecular orbital levels by adjusting the coulomb and resonance integral values (see Table S6, ESI†). The molecular structure of the CNDs (Fig. 5C) was generated from a graphite structure surrounded by amorphous carbon atoms and surface functional groups, which were chosen to correspond to the atomic ratio of C : O : N obtained by XPS. The core size was then increased until a HOMO–LUMO energy gap of 2.07 eV was reached. At the same given parameters, different orbital energy levels (LUMO+2, LUMO+1, LUMO, and HOMO, HOMO−1, HOMO−2) could be obtained; see Fig. S11, ESI†.[30] The calculated LUMO (−3.71 eV) and HOMO (−5.78 eV) electronic state energies of the molecular CND are consistent with that obtained by the electrochemical experiments (about −3.75 ± 0.04 and −5.84 ± 0.04 eV).

The molecular orbital model has been applied to understand the fluorescence properties of graphene oxide nanodots previously,[58,59] and the dominant fluorescence mechanism was found to originate from the electronic transitions among/between the non-oxidized carbon regions and the boundary of oxidized carbon atom regions involving the functionalized groups C–O, C=O and COOH. Compared to the graphene oxide quantum dots, previous studies indicate that the CNDs have a less defined π-electron core and a larger proportion of functional groups, thus little quantum confinement effect on photoluminescence.[60] In this work, the π-core region of the CNDs is small, as determined from the XRD data, yet the CND size distribution is mostly uniform. The molecular orbital energy levels that are derived from Hückel theory show good agreement with the observed fluorescence of the CNDs between 400 nm (photo energy of 3.10 eV) and 600 nm (photo energy of 2.06 eV) (Fig. 2A) which may correspond to the potential electronic transitions from LUMO to HOMO (gap of 2.07 eV), to HOMO−1 (energy difference of 3.92 eV), and to HOMO−2 (3.94 eV), and/or from LUMO+1 to HOMO (2.65 eV), and from LUMO+2 to HOMO (2.66 eV). Here, the responsible atom groups resulting in the potential electronic transitions include non-oxidized carbon (C=C), the oxidized carbon (C=O and C–O), and functionalized carbon (COOH), with electronic transition moments for C=C, C=O, C–O and O–H being 3.24 D, 2.93 D, 3.43 D and 2.30 D, respectively (details in ESI† and Table S7). Since the photoluminescence could be proposed to be proportional to the time constant and the number of electrons from high to low energy levels, here, the Hückel model treatment combines the conjugated π states (C=C) with the functional groups (C=O, C–O, and O=C–OH), which can be dominant factors in the excitation-dependent emission of CNDs. Note that the electric vector is

aligned parallel with (or perpendicular to) the transition moment of the bonds resulting in higher (or lower) light absorbance. This indirectly affects the electronic transition probability and photoluminescence properties.[58,61] For the photoluminescence origin of amorphous CNDs, the light emission characteristic has been generally ascribed to surface-related defect sites and radiative recombination of excited surface states.[60] In this study, based on the energy gap calculation and the observation of the fluorescence-based spectro-electrochemistry analysis, we propose that the photoluminescence arises from a combination of the C=C core regions, the surface functional groups (C=O, C–O, and COOH), and the surface electronic state transitions. However, the question regarding the effect of the C=C core-region, *e.g.* the size dependent quantum confinement, and its contribution to the origin of fluorescence from such microwave synthesized CNDs is open; and it may be explored by controlling the core sizes while maintaining the surface states.

Conclusions

A new fluorescence spectroelectrochemistry approach was developed to investigate the real-time electrochemical-fluorescence properties of microwave synthesized CNDs, and a chemically reversible redox couple was used to reveal the influence of redox chemistry on the optoelectronic properties of the CNDs. The effect of different excitation wavelengths from a fluorescence spectrophotometer on the photocurrent generated by the CND modified gold slide electrodes upon different applied bias voltages was investigated systematically, suggesting wavelength dependence of photocurrent generation from the CNDs as electron donors to the gold electrode. The optical band gap of the CNDs obtained by the UV-Vis absorption spectrum is in reasonable agreement with the HOMO–LUMO energy gap found from electrochemical measurements. A theoretical Hückel model was adopted to obtain the molecular-like CND structure and was fitted to match the experimental energy gap between HOMO and LUMO energy levels. From both experimental and theoretical energy gap analysis and the observation of the fluorescence-based spectroelectrochemistry, the excitation dependent fluorescence of the CNDs may be attributed to a combination of the core C=C, surface functionalities (C=O, C–O, and COOH), and/or surface electronic state transitions. This study provides a new perspective on the optoelectronic properties of the CNDs, which should motivate and facilitate their broad applications in biomedicine (*e.g.* bioimaging, antioxidation) and photoelectric devices.

Authors contributions

JW conceived and developed the concept; ZZ and WZ designed the research plan and conducted most experiments; DMA did the bioimaging studies; BB conducted the XPS experiments; AS performed the AFM experiments; TM built the gold slide; YL, ZJ and HC performed XRD and UV-Vis experiments; and DHW supervised the XPS and energy gap analysis. JW supervised the whole research. ZZ, WZ and JW co-wrote the manuscript; all authors discussed the results and commented on the manuscript.

Acknowledgements

JW *et al.* at Joint School of Nanoscience and Nanoengineering (JSNN) acknowledge the partial support by the National Heart, Lung, and Blood Institute of the National Institutes of Health

under Award Number R15HL129212. This work was performed at the JSNN, a member of Southeastern Nanotechnology Infrastructure Corridor (SENIC) and National Nanotechnology Coordinated Infrastructure (NNCI), which is supported by the National Science Foundation (ECCS-1542174). DHW and BB acknowledge support through the US Department of Energy (Grant# ER46430).

Notes and references

1. S. Zhu , Q. Meng , L. Wang , J. Zhang , Y. Song , H. Jin , K. Zhang , H. Sun , H. Wang and B. Yang , *Angew. Chem., Int. Ed.*, 2013, **52** , 3953 —3957.
2. S. Y. Lim , W. Shen and Z. Gao , *Chem. Soc. Rev.*, 2015, **44** , 362 —381.
3. X. T. Zheng , A. Ananthanarayanan , K. Q. Luo and P. Chen , *Small*, 2015, **11** , 1620 —1636.
4. Y. Wang and A. Hu , *J. Mater. Chem. C*, 2014, **2** , 6921 —6939.
5. X. Li , M. Rui , J. Song , Z. Shen and H. Zeng , *Adv. Funct. Mater.*, 2015, **25** , 4929 —4947.
6. Q. Xu , J. Wei , J. Wang , Y. Liu , N. Li , Y. Chen , C. Gao , W. Zhang and T. S. Sreeprased , *RSC Adv.*, 2016, **6** , 28745 —28750.
7. L. Wang , S.-J. Zhu , H.-Y. Wang , S.-N. Qu , Y.-L. Zhang , J.-H. Zhang , Q.-D. Chen , H.-L. Xu , W. Han , B. Yang and H.-B. Sun , *ACS Nano*, 2014, **8** , 2541 —2547.
8. K. Hola , A. B. Bourlinos , O. Kozak , K. Berka , K. M. Siskova , M. Havrdova , J. Tucek , K. Safarova , M. Otyepka , E. P. Giannelis and R. Zboril , *Carbon*, 2014, **70** , 279 —286.
9. Z. Luo , P. M. Vora , E. J. Mele , A. T. C. Johnson and J. M. Kikkawa , *Appl. Phys. Lett.*, 2009, **94** , 111909.
10. S. N. Baker and G. A. Baker , *Angew. Chem., Int. Ed.*, 2010, **49** , 6726 —6744.
11. S. K. Cushing , M. Li , F. Huang and N. Wu , *ACS Nano*, 2014, **8** , 1002 —1013.
12. S. Zhu , J. Shao , Y. Song , X. Zhao , J. Du , L. Wang , H. Wang , K. Zhang , J. Zhang and B. Yang , *Nanoscale*, 2015, **7** , 7927 —7933.
13. G. Eda , Y.-Y. Lin , C. Mattevi , H. Yamaguchi , H.-A. Chen , I. S. Chen , C.-W. Chen and M. Chhowalla , *Adv. Mater.*, 2010, **22** , 505 —509.
14. K. Krishnamoorthy , M. Veerapandian , R. Mohan and S.-J. Kim , *Appl. Phys. A: Mater. Sci. Process.*, 2012, **106** , 501 —506.
15. H. Li , X. He , Z. Kang , H. Huang , Y. Liu , J. Liu , S. Lian , C. H. A. Tsang , X. Yang and S.-T. Lee , *Angew. Chem., Int. Ed.*, 2010, **49** , 4430 —4434.
16. Y.-P. Sun , B. Zhou , Y. Lin , W. Wang , K. A. S. Fernando , P. Pathak , M. J. Meziani , B. A. Harruff , X. Wang , H. Wang , P. G. Luo , H. Yang , M. E. Kose , B. Chen , L. M. Veca and S.-Y. Xie , *J. Am. Chem. Soc.*, 2006, **128** , 7756 —7757.
17. L. Cao , M. J. Meziani , S. Sahu and Y.-P. Sun , *Acc. Chem. Res.*, 2013, **46** , 171 —180.
18. R. Liu , D. Wu , S. Liu , K. Koynov , W. Knoll and Q. Li , *Angew. Chem., Int. Ed.*, 2009, **48** , 4598 —4601.
19. C. Lei , D. Hu and E. J. Ackerman , *Chem. Commun.*, 2008, 5490 —5492.
20. Y.-L. Chang , R. E. Palacios , F.-R. F. Fan , A. J. Bard and P. F. Barbara , *J. Am. Chem. Soc.*, 2008, **130** , 8906 —8907.
21. S. Zaleski , M. F. Cardinal , J. M. Klingsporn and R. P. Van Duyne , *J. Phys. Chem. C*, 2015, **119** , 28226 —28234.
22. Z. Zeng , Y. Liu and J. Wei , *TrAC, Trends Anal. Chem.*, 2016, **75** , 162 —173.

23. Y. Gründer , J. F. W. Mosselmans , S. L. M. Schroeder and R. A. W. Dryfe , *J. Phys. Chem. C*, 2013, **117** , 5765 —5773.
24. B. Gadgil , P. Damlin , E. Dmitrieva , T. Aaritalo and C. Kvarnstrom , *RSC Adv.*, 2015, **5** , 42242 —42249.
25. S. Qu , X. Wang , Q. Lu , X. Liu and L. Wang , *Angew. Chem., Int. Ed.*, 2012, **51** , 12215 —12218.
26. M. Sanders , Y. Lin , J. Wei , T. Bono and R. G. Lindquist , *Biosens. Bioelectron.*, 2014, **61** , 95 —101.
27. Z. Zeng , X. Shi , T. Mabe , S. Christie , G. Gilmore , A. W. Smith and J. Wei , *Anal. Chem.*, 2017, **89** , 5221 —5229.
28. D. Yu , Y. Yang , M. Durstock , J.-B. Baek and L. Dai , *ACS Nano*, 2010, **4** , 5633 —5640.
29. C. M. Cardona , W. Li , A. E. Kaifer , D. Stockdale and G. C. Bazan , *Adv. Mater.*, 2011, **23** , 2367 —2371.
30. Y. Liu , S. Jiang , K. Glusac , D. H. Powell , D. F. Anderson and K. S. Schanze , *J. Am. Chem. Soc.*, 2002, **124** , 12412 —12413.
31. H. Hou , C. E. Banks , M. Jing , Y. Zhang and X. Ji , *Adv. Mater.*, 2015, **27** , 7861 —7866.
32. C. S. Lim , K. Hola , A. Ambrosi , R. Zboril and M. Pumera , *Electrochem. Commun.*, 2015, **52** , 75 —79.
33. S. Muthulingam , K. B. Bae , R. Khan , I.-H. Lee and P. Uthirakumar , *RSC Adv.*, 2015, **5** , 46247 —46251.
34. Q. Cui , J. Xu , X. Wang , L. Li , M. Antonietti and M. Shalom , *Angew. Chem., Int. Ed.*, 2016, **55** , 3672 —3676.
35. M. Zhang , L. Bai , W. Shang , W. Xie , H. Ma , Y. Fu , D. Fang , H. Sun , L. Fan , M. Han , C. Liu and S. Yang , *J. Mater. Chem.*, 2012, **22** , 7461 —7467.
36. J. Zhang , F. Abbasi and J. Claverie , *Chem. – Eur. J.*, 2015, **21** , 15142 —15147.
37. T. V. Cuong , V. H. Pham , Q. T. Tran , S. H. Hahn , J. S. Chung , E. W. Shin and E. J. Kim , *Mater. Lett.*, 2010, **64** , 399 —401.
38. Z. Luo , Y. Lu , L. A. Somers and A. T. C. Johnson , *J. Am. Chem. Soc.*, 2009, **131** , 898 —899.
39. H. Zhu , X. Wang , Y. Li , Z. Wang , F. Yang and X. Yang , *Chem. Commun.*, 2009, 5118 —5120.
40. S. K. Bhunia , A. Saha , A. R. Maity , S. C. Ray and N. R. Jana , *Sci. Rep.*, 2013, **3** , 1473.
41. X. Li , S. Zhang , S. A. Kulinich , Y. Liu and H. Zeng , *Sci. Rep.*, 2014, **4** , 4976.
42. M. Fu , F. Ehrat , Y. Wang , K. Z. Milowska , C. Reckmeier , A. L. Rogach , J. K. Stolarczyk , A. S. Urban and J. Feldmann , *Nano Lett.*, 2015, **15** , 6030 —6035.
43. Z.-C. Yang , M. Wang , A. M. Yong , S. Y. Wong , X.-H. Zhang , H. Tan , A. Y. Chang , X. Li and J. Wang , *Chem. Commun.*, 2011, **47** , 11615 —11617.
44. C. A. Schroll , S. Chatterjee , W. R. Heineman and S. A. Bryan , *Anal. Chem.*, 2011, **83** , 4214 —4219.
45. D. Ibañez , J. Garoz-Ruiz , A. Heras and A. Colina , *Anal. Chem.*, 2016, **88** , 8210 —8217.
46. M. Amjadi , J. L. Manzoori , T. Hallaj and M. H. Sorouraddin , *Spectrochim. Acta, Part A*, 2014, **122** , 715 —720.
47. V. Strauss , J. T. Margraf , C. Dolle , B. Butz , T. J. Nacken , J. Walter , W. Bauer , W. Peukert , E. Spiecker , T. Clark and D. M. Guldi , *J. Am. Chem. Soc.*, 2014, **136** , 17308 —17316.

48. J. Wei , H. Liu , A. R. Dick , H. Yamamoto , Y. He and D. H. Waldeck , *J. Am. Chem. Soc.*, 2002, **124** , 9591 —9599.
49. A. Kongkanand , K. Tvrdy , K. Takechi , M. Kuno and P. V. Kamat , *J. Am. Chem. Soc.*, 2008, **130** , 4007 —4015.
50. R. Miao , Z. Luo , W. Zhong , S.-Y. Chen , T. Jiang , B. Dutta , Y. Nasr , Y. Zhang and S. L. Suib , *Appl. Catal., B*, 2016, **189** , 26 —38.
51. W. Wu , L. Zhan , W. Fan , J. Song , X. Li , Z. Li , R. Wang , J. Zhang , J. Zheng , M. Wu and H. Zeng , *Angew. Chem.*, 2015, **127** , 6640 —6644.
52. Y. Hao , Z. Gan , X. Zhu , T. Li , X. Wu and P. K. Chu , *J. Phys. Chem. C*, 2015, **119** , 2956 —2962.
53. A. Mohite , J.-T. Lin , G. Sumanasekera and B. W. Alphenaar , *Nano Lett.*, 2006, **6** , 1369 —1373.
54. G. Likhtenshtein *Electron Spin Interactions in Chemistry and Biology* , Springer International Publishing, 2016.
55. M. Harb *Phys. Chem. Chem. Phys.*, 2015, **17** , 25244 —25249.
56. D. Moses , J. Wang , A. J. Heeger , N. Kirova and S. Brazovski , *Proc. Natl. Acad. Sci. U. S. A.*, 2001, **98** , 13496 —13500.
57. Y. Zou , A. Najari , P. Berrouard , S. Beaupré , B. Réda Aïch , Y. Tao and M. Leclerc , *J. Am. Chem. Soc.*, 2010, **132** , 5330 —5331.
58. J. Shang , L. Ma , J. Li , W. Ai , T. Yu and G. G. Gurzadyan , *Sci. Rep.*, 2012, **2** , 792.
59. C. Galande , A. D. Mohite , A. V. Naumov , W. Gao , L. Ci , A. Ajayan , H. Gao , A. Srivastava , R. B. Weisman and P. M. Ajayan , *Sci. Rep.*, 2011, **1** , 85.
60. A. Cayuela , M. L. Soriano , C. Carrillo-Carrion and M. Valcarcel , *Chem. Commun.*, 2016, **52** , 1311 —1326.
61. T. Itoh *Chem. Rev.*, 2012, **112** , 4541 —4568.

Footnotes

† Electronic supplementary information (ESI) available: Additional AFM, XPS data, zeta potential, quantum yield, cell imaging, control results of CNDs and details of three kinds of energy gap calculations. See DOI: 10.1039/c7cp02875j